Science Advances

AAAS

advances.sciencemag.org/cgi/content/full/1/8/e1500224/DC1

Supplementary Materials for

Unraveling metamaterial properties in zigzag-base folded sheets

Maryam Eidini and Glaucio H. Paulino

Published 18 September 2015, *Sci. Adv.* **1**, e1500224 (2015)
DOI: 10.1126/sciadv.1500224

The PDF file includes:

Other Supplementary Material for this manuscript includes the following:
(available at advances.sciencemag.org/cgi/content/full/1/8/e1500224/DC1)

Movie S1 (.mov format). In-plane behavior of the patterns.
Movie S2 (.mov format). A cellular folded metamaterial made by stacking seven layers of a 3×3 sheet of BCH_2 pattern with two different geometries.
Movie S3 (.mov format). Out-of-plane behavior of the patterns.

Supplementary Text

1- Geometry, pattern tessellation and combination

The geometry of BCH_n (Basic unit Cell with Hole) is described in the main text and is shown in Fig. 2A. By combining BCH_n with row/rows of small and/or large parallelograms with the same angle ϕ, we can obtain numerous unit cells. A few configurations are presented in Fig. S1. The tessellations or/and combinations of tessellation of these cells having the same angle ϕ can result in a new metamaterial. For example, the patterns shown in Fig. 3 C and D are obtained by tessellations of the unit cells presented in Fig. S1D.

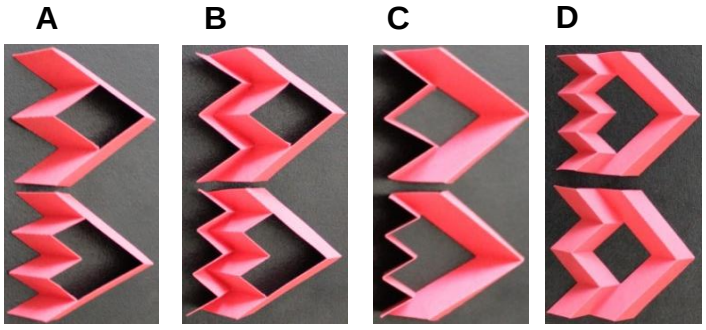

Fig. S1. BCH_2, BCH_3, and their combinations with rows of small and/or large parallelograms. (**A**) A BCH_2 and a BCH_3. (**B**) A BCH_2 and a BCH_3 combined with a row of small parallelograms with the same geometry as the one used in the corresponding BCH. (**C**) A BCH_2 and a BCH_3 combined with a row of large parallelograms with the same geometry as the one used in their corresponding BCH. (**D**) A BCH_2 and a BCH_3 combined with rows of small and large parallelograms with the same geometry as the one used in their corresponding BCH.

2- Kinematics of a folded one-DOF zigzag strip

A one-DOF zigzag strip of parallelogram facets can be decomposed into *V*-shapes. We show that the kinematics of a properly constrained *V*-shape (see Fig. 1B), as described below, is a function of an angle in the horizontal ***xy***-plane. The constraints on the *V*-shape (Fig. 1B) are applied to simulate similar conditions to those of the *V*-shapes in the Miura-ori sheet, i.e., to create a one-DOF planar mechanism. Hence, to remove the rigid body motions associated with the translational and rotational DOFs, we constrain all translational DOFs of the point *A* and assume that the edges *AB* and *BC* of the facets move in the ***xy***-plane, and that the projected length of the edge *AD* in the ***xy***-plane remains along the ***x***-axis (i.e., point *D* moves in the ***xz***-plane). With this set up, the *V*-shape has only one planar DOF. The expressions defining the geometry of the *V*-shape are given by

$$\ell_v = a\frac{\cos\alpha}{\cos\phi} \qquad w_v = 2b\sin\phi \tag{1}$$

where ℓ_v is the projected length of the edges *a* in the ***xy***-plane and in the ***x*** direction; w_v is the width of the semi-folded *V*-shape in the ***xy***-plane and along the ***y*** direction; ϕ is an angle

in the ***xy***-plane between the edge *b* and the ***x***-axis (see Fig. 1B). The in-plane Poisson's ratio of the system is given by

$$\left(\upsilon_{w,\ell}\right)_V = -\frac{\varepsilon_{\ell_v}}{\varepsilon_{w_v}} = -\frac{d\ell_v / \ell_v}{dw_v / w_v} = -\tan^2\phi \qquad (2)$$

3- Number of degrees of freedom of the patterns

For the case of n=2, i.e., for the unit cell of BCH_2 pattern shown in Fig. 2A, and for a given geometry of the facet, the geometry of the unit cell implies that it can be defined based on only one fold angle (i.e., similarly to Miura-ori (*1*), we can write the relations between all degrees of freedom (DOFs) based on only one fold angle, e.g., the angle ϕ). Hence, the unit cell of BCH_2 has only one DOF. On the other hand, implicit formation of the structure of the Miura-ori unit cell with one DOF mechanism between two adjoining unit cells, as shown in Fig. S2A, imposes the whole pattern to have only one DOF. The conclusion is further verified using numerical calculation of the number of DOFs as described in Section (7-1).

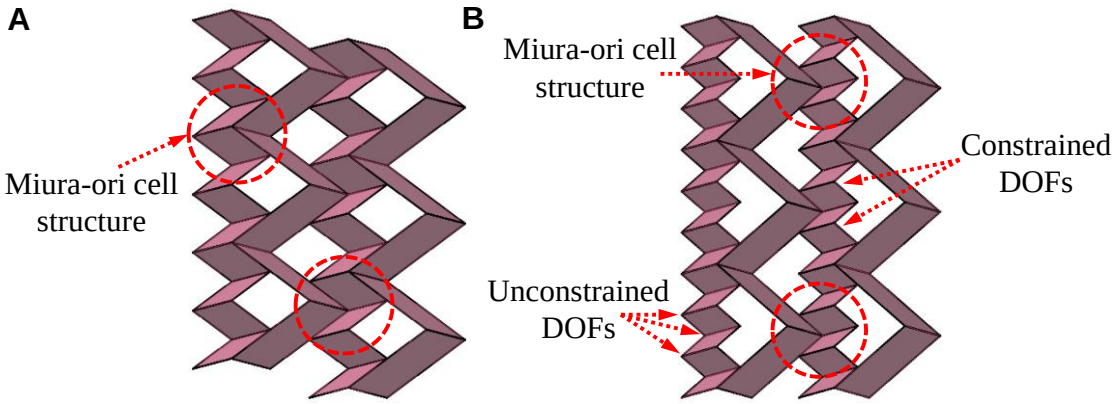

Fig. S2. Constrained DOF by implicit formation of the structure of the Miura-ori unit cell between adjoining unit cells of BCH_2 and BCH_3 in the pattern. (**A**) The Miura-ori unit cell structure formed implicitly in the tessellation makes the whole BCH_2 pattern fold with one-DOF planar mechanism. (**B**) In the symmetric tessellation of identical BCH_3, except for the small parallelogram facets of the first row, all other independent DOFs in the unit cell of BCH_3 are constrained by the structure of the Miura-ori cell formed between two adjoining unit cells.

In general, from the numerical model described in Section (7-1) and for rigid origami behavior, the unit cell of BCH_n (Fig. S1A) has 2n-3 DOFs. However, adding one row of small parallelogram facets to the BCH_n (e.g., Fig. S1B), i.e., creating a complete row of Miura-ori unit cells with the small parallelogram facets, reduces the DOFs of the cell to 1 irrespective of the number of n. Hence, tessellation of the unit cells shown in Fig. S1B can create patterns with one DOF planar mechanism (e.g., Fig. 3E).

For the symmetric tessellation of BCH_3, as presented in Fig. S2B, except for the first row of small parallelogram facets, all other independent DOFs in the unit cell of BCH_3 are constrained by the implicit formation of the structure of Miura-ori cell between two adjoining unit cells. Hence, the pattern of BCH_3, shown in Fig. S2B, due to existence of unconstrained DOFs in the first row of small parallelogram facets, has more than one DOF. However, adding one row of small parallelogram facets and, accordingly, creating the row of Miura-ori cells with small parallelogram facts can reduce the DOF of the whole system to one (e.g., Fig. 3B).

4- In-plane stretching response of BCH_n sheets

4-1- Poisson's ratio

A 5x4 sheet of BCH_2 along with its corresponding Miura-ori sheet containing the same geometry of facets and fold angle (*a*, *b*, α and ϕ are identical in both models) is shown in Fig. 4A. The Poisson's ratio υ_z for both sheets can be obtained from the following relation

$$\left(\upsilon_{w\ell}\right)_z = -\frac{\varepsilon_\ell}{\varepsilon_w} = -\frac{d\ell/\ell}{dw/w} \tag{3}$$

in which ℓ is the projected length of the zigzag strips in the ***xy***-plane and parallel to the **x**-axis (*i.e.*, the projected lengths of the zigzag strips along any arbitrary lines of ***x'-x'*** in the ***xy*** plane and parallel to the ***x***-axis intersecting a complete tessellation). Hence, for a sheet with m_1 rows, ℓ is equal to m_1 times the projected lengths of the strips in the unit cell shown in Fig. 2A. From Fig. 4A, the importance of considering the end-to-end dimensions to obtain the Poisson's ratio for folded sheets is more pronounced in sheets with holes because both sheets have the same υ_z despite having different lengths along the ***x***-axis. Another example, showing the relevance of the end-to-end dimensions to obtain Poisson's ratio of folded sheets is presented in Fig. S3, where two identical 2x2 Miura-ori sheets are shown. Moreover, 2 rows of small Miura-ori cells with equal υ_z are also attached to the left-hand sample as shown in the figure. Therefore, from the figure, considering the end-to-end dimensions to obtain Poisson's ratio in the left system is obvious. For the limit cases of very large number of small cells, as well as very small length of *a* for small cells, *i.e.*, $n \to \infty$ and $a_s \to 0$ (See Fig. S4 for the geometry of Miura-ori cell), the rows of small Miura-ori cells approach the lines defining the end-to-end dimension for the 2x2 Miura-ori sheet shown on the right-hand image.

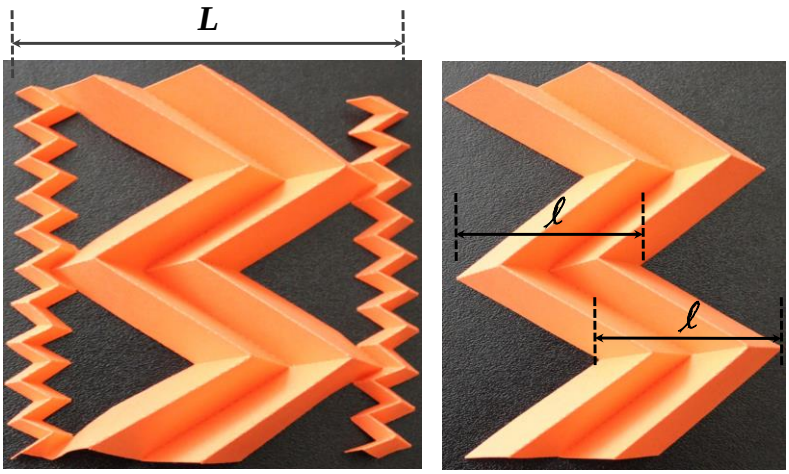

Fig. S3. Concept of Poisson's ratio considering end-to-end dimensions. Figure shows two identical 2x2 Miura-ori tessellations. The 2 rows of small Mira-ori cells with the same υ_z as that of the 2x2 sheet are attached to the left sample. Length *b* of the small cells are 1/5 of that of the large cells (*i.e.*, the number of small cells per each large cell is 5 (*n*=5)).

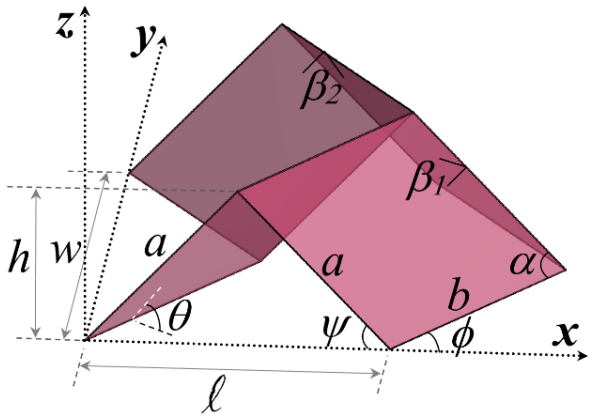

Fig. S4. Geometry of a Miura-ori cell.

The Poisson's ratio of a BCH_n sheet, using the end-to-end dimensions, is given in expression (6) of the main text. From the relation, when $\kappa \cdot \lambda \cos\alpha < \cos^2\phi$, υ_{e-e} is positive and for $\kappa \cdot \lambda \cos\alpha > \cos^2\phi$, υ_{e-e} is negative. Moreover, for a Miura-ori (*n*=1) sheet, we have

$$\left(\upsilon_{WL}\right)_{e-e} = -\tan^2\phi \frac{2m_1\lambda\cos\alpha - \cos^2\phi}{2m_1\lambda\cos\alpha + \cos^2\phi} \tag{4}$$

Hence, for a Miura-ori sheet, if $m_1 \to \infty$, then υ_{e-e} approaches υ_z (*i.e.*, $-\tan^2\phi$). Notice that from the relation above, even a Miura-ori unit cell (i.e., $m_1 = 1$) can have positive Poisson's ratio for some ranges.

For a sheet of BCH_2, we have

$$\left(\upsilon_{WL}\right)_{e-e} = -\tan^2\phi \frac{\frac{4m_1}{m_1+1}\lambda\cos\alpha - \cos^2\phi}{\frac{4m_1}{m_1+1}\lambda\cos\alpha + \cos^2\phi} \tag{5}$$

From the relation above, for a sheet of BCH_2, while comparing υ_z with υ_{e-e}, the shift towards positive Poisson's ratio in υ_{e-e} is mainly the effect of the holes, and thus the difference between υ_z and υ_{e-e} does not disappear (see Fig. 5) when the length of the sheet approaches infinity ($m_1 \to \infty$). Table S1 summarizes the main points on the in-plane Poisson's ratio of the class of zigzag-base folded materials.

Table S1. Main points of the in-plane Poisson's ratio of the class of zigzag-base folded metamaterials.

Using projected length of the zigzag strips $\upsilon_z = -\frac{d\ell/\ell}{dw/w} = -\tan^2\phi$	**Using the end-to-end dimensions of a sheet** $\upsilon_{e-e} = -\frac{dL/L}{dW/W}$
❖ By introducing BCH_n patterns, our work shows that the value is an inherent property of the class of one-DOF zigzag-base folded materials, and is always negative and is a function of the angle ϕ. ❖ Provides insight on the kinematics and thus on how to create zigzag-base foldable metamaterials. ❖ It has been used in the literature (*1*) as the Poisson's ratio of the Miura-ori, to describe the stacking of the Miura-ori sheets. ❖ By explicitly associating the value to each zigzag, and thus by changing the scale of the zigzags in the patterns, we have created the BCH_n patterns.	❖ The value captures the size change of the sheets, and is a function of the geometry of the facets, tessellation, and the angle ϕ. It can be positive depending on the geometry. ❖ For an infinite tessellation of a regular sheet, it captures the Poisson's ratio of a repeating unit cell. ❖ The in-plane Poisson's ratio of a repeating unit cell of the Miura-ori sheet, obtained in this way, is equal to υ_z. ❖ For the Miura-ori, considering the end-to-end is to simply capture the edge effect (*32*). However, for the BCH_n patterns, it is to capture the effect of the holes in the patterns.

4-2- Stretching stiffness

4-2-1- BCH_2

In this section, we derive the in-plane stiffness of the BCH_2 in the ***x*** and ***y*** directions. For this purpose, an alternative parameterization for BCH_2 (the unit cell is shown in Fig. 2A) based on the dihedral angles between the rigid facets is used, which is similar to the equations of reference (*3*) for Miura-ori cell. To better compare the results, we keep the same symbols as those given for Miura-ori (*3*), provided that they are consistent with the symbols used in this work. Therefore,

$$\ell = 2a\zeta \qquad w = 2b\xi \qquad h = a\zeta \tan\alpha \cos(\beta_1/2) \tag{6}$$

in which

$$\xi = \sin\alpha \sin\left(\beta_1/2\right) \qquad \text{and} \qquad \zeta = \cos\alpha\left(1-\xi^2\right)^{-1/2} \tag{7}$$

The potential energy of a BCH_2 (see Fig. 2A), subjected to uniaxial force in the ***x*** direction, can be obtained from

$$H = U + \Omega \tag{8}$$

in which U and Ω are elastic energy and potential of the applied load, respectively that are given by

$$U = \frac{1}{2}k\left(4a(\beta_1-\beta_{1_0})^2 + b(\beta_2-\beta_{2_0})^2\right) \tag{9}$$

$$\Omega = -\int_{\beta_{1_0}}^{\beta_1} f_x \frac{d\ell}{d\beta_1'}\, d\beta_1' \tag{10}$$

where k is the rotational hinge spring constant per unit length ($k=K_{fold}$). Setting the condition $\partial H/\partial\beta_1 = 0$, the external force at equilibrium f_x can be obtained from

$$f_x = \frac{dU/d\beta_1}{d\ell/d\beta_1} = \frac{2k}{\cos\alpha\sin^2\alpha}\left(\frac{4(\beta_1-\beta_{1_0})\left(1-\xi^2\right)^{3/2} + \frac{b}{a}\cdot(\beta_2-\beta_{2_0})\cos\alpha\left(1-\xi^2\right)^{1/2}}{\sin\beta_1}\right) \tag{11}$$

Notice that K_x is obtained from the following expression

$$K_x(\alpha,\beta_{1_0}) = \left.\frac{df_x}{d\ell}\right|_{\beta_{1_0}} = \left.\frac{df_x}{d\beta_1}\cdot\frac{d\beta_1}{d\ell}\right|_{\beta_{1_0}} \tag{12}$$

$$K_x(\alpha,\beta_{1_0}) = \left(2k\cdot\frac{4a(1-\xi_0{}^2)^2 + b\cos^2\alpha}{a(1-\xi_0{}^2)^{1/2}\cos\alpha\sin^2\alpha\sin\beta_{1_0}}\right)\left(\frac{8a^2\cos\alpha}{\ell^3\sqrt{1-\frac{4a^2\cos^2\alpha}{\ell^2}}\sqrt{\frac{4a^2}{\ell^2}-1}}\right) \tag{13}$$

where $\xi_0 = \xi\left(\alpha,\beta_{1_0}\right)$. The contour plot of the stiffness ratio in the ***x*** direction (K_x/k) is shown in Fig. S5A for a unit cell with *a=b=1*, in terms of the facet angle α and fold angle β_1.

Similarly, for the ***y*** direction:

$$f_y = \frac{dU/d\beta_1}{dw/d\beta_1} = \frac{k}{b\sin\alpha}\cdot\frac{4a(\beta_1-\beta_{1_0}) + b(\beta_2-\beta_{2_0})\left(\frac{\cos\alpha}{1-\xi^2}\right)}{\cos\left(\beta_1/2\right)} \tag{14}$$

$$K_y(\alpha,\beta_{1_0}) = \frac{df_y}{dw}\bigg|_{\beta_{1_0}} = \frac{df_y}{d\beta_1}\cdot\frac{d\beta_1}{dw}\bigg|_{\beta_{1_0}} \tag{15}$$

$$K_y(\alpha,\beta_{1_0}) = \frac{k}{b}\left(\frac{4a(1-\xi_0{}^2)^2 + b\cos^2\alpha}{(1-\xi_0{}^2)^2\sin\alpha\cos(\beta_{1_0}/2)}\right)\left(\frac{2}{\sqrt{4b^2\sin^2\alpha - w^2}}\right) \tag{16}$$

The contour plot of the stiffness in the ***y*** direction is shown in Fig. S5B for a unit cell with *a=b=1* in terms of the facet and fold angles, α and β_1, respectively.

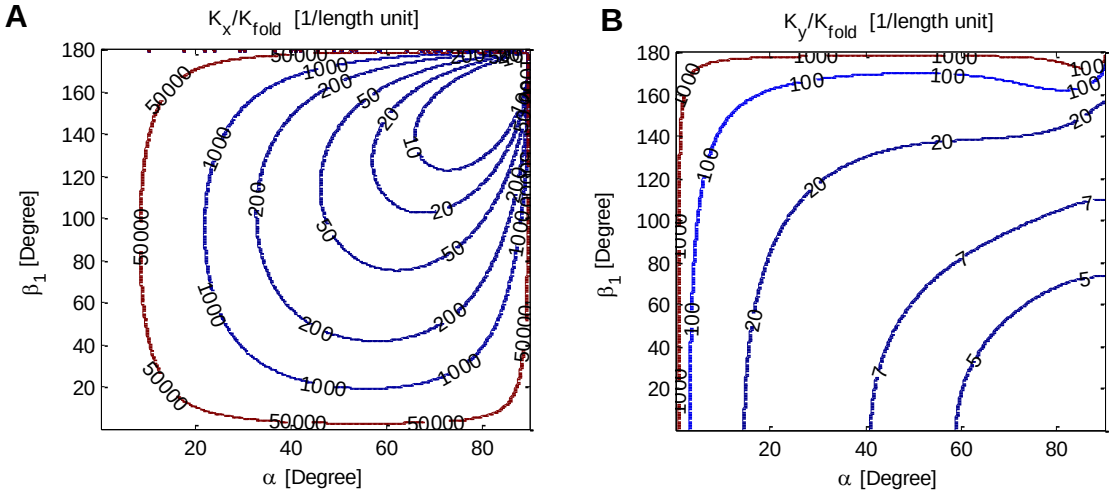

Fig. S5. In-plane stiffness for BCH_2 with *a* = *b* = *1*. (**A**) K_x/k. (**B**) K_y/k.

Note that to compare the in-plane stiffness results with those of the Miura-ori, we considered a measure of the in-plane stiffness of the BCH_2 which is equivalent to the load making the unit displacement in the zigzag strips of the unit cell (i.e., the length of the zigzag strips are used in the derivations).

4-2-2- Classical Miura-ori

The in-plane stretching stiffness in the ***x*** direction for Miura-ori cell is obtained by equation (12), which results in

$$K_x(\alpha,\beta_{1_0}) = \left(4k\frac{a(1-\xi_0{}^2)^2 + b\cos^2\alpha}{a(1-\xi_0{}^2)^{1/2}\cos\alpha\sin^2\alpha\sin\beta_{1_0}}\right)\left(\frac{8a^2\cos\alpha}{\ell^3\sqrt{1-\frac{4a^2\cos^2\alpha}{\ell^2}}\sqrt{\frac{4a^2}{\ell^2}-1}}\right) \tag{17}$$

The second term within brackets is missing in Ref. (*3*). Similarly, the stretching stiffness in the ***y*** direction is obtained by equation (15), which results in

$$K_y(\alpha,\beta_{1_0})=\left(2k\frac{a(1-\xi_0{}^2)^2+b\cos^2\alpha}{b(1-\xi_0{}^2)^2\sin\alpha\cos(\beta_{1_0}/2)}\right)\left(\frac{2}{\sqrt{4b^2\sin^2\alpha-w^2}}\right) \tag{18}$$

Notice that K_x/k and K_y/k are not dimensionless, and thus K_x and K_y have dimension of in-plane stretching stiffness (*38*).

4-2-3- In-plane stiffness of BCH_2 compared with its corresponding Miura-ori cell

Figure 5 shows the ratio of the in-plane stiffness of the Miura-ori cell in the ***x*** and ***y*** directions to those of the BCH_2, for various ratios of *a/b*. The ratio is equal for both ***x*** and ***y*** directions because only the numerators of the first term in the planar stiffness relations change from BCH_2 to Miura-ori cell, and the numerators are equal in both planar rigidities of ***x*** and ***y*** directions for a specific unit cell.

5- BCH_n-based cellular folded metamaterial

Similar sheets with different heights, while possessing the same υ_z, can be stacked and attached together along joining fold lines to make a cellular folded metamaterials (see Fig. 3 G and H and and movie S2). The fold geometry can change from layer to layer, but assuming stacking of the patterns using 2 layers of A and B (*1*), and by equating the external dimensions as well as υ_z for both layers of A and B, respectively, we have

$$b_B=b_A \qquad a_B=a_A\frac{\cos\alpha_A}{\cos\alpha_B} \tag{19}$$

$$\theta_B=\arccos\left(\cos\theta_A\frac{\tan\alpha_A}{\tan\alpha_B}\right) \tag{20}$$

where the geometry of the layer B can be obtained based on that of the layer A. It is worth noting that meeting the above equations, for the stacking of the layers, results in the sheets possessing identical υ_{e-e}, as shown by the following relations:

$$\left(\upsilon_{e-e}\right)_A=-\tan^2\phi\frac{\kappa\frac{a_A}{b_A}\cos\alpha_A-\cos^2\phi}{\kappa\frac{a_A}{b_A}\cos\alpha_A+\cos^2\phi}=-\tan^2\phi\frac{\kappa\frac{a_B}{b_B}\cos\alpha_B-\cos^2\phi}{\kappa\frac{a_B}{b_B}\cos\alpha_B+\cos^2\phi}=\left(\upsilon_{e-e}\right)_B \tag{21}$$

This result further emphasizes the relevance of defining the end-to-end Poisson's ratio for the zigzag-base folded sheet metamaterials.

The angle θ for the stacked samples shown in Fig. 3G is positive for both sheets, *i.e.* $\theta_A,\theta_B\in[0,\pi/2]$. This form of stacking may be applied as impact absorbing devices (*36*).

Considering the angle θ for one alternating layer being negative, *i.e.* $\theta_A\in[-\pi/2,\,0]$ results in a new metamaterial in which the layers can be connected along joining fold lines using adhesive (Fig. 3H). In this way of stacking, the heights for two successive layers can be

identical.

6- Experimental Responses of the Patterns

6-1- In-plane behavior

Under in-plane extension, the patterns, for large geometric ranges (see the analytical model in the main text), exhibit negative Poisson's ratios. Simple in-plane experimental tests confirm that, for most geometric ranges, the patterns exhibit negative Poisson's ratio (movie S1).

6-2- Out-of-plane behavior

Under bending, this class of patterns folded from various types of papers exhibit anticlastic (saddle-shaped) curvature (see Fig. 7A, Fig. S6A, Fig. S7A, Fig. S8A and movie S3) which is an adopted curvature by conventional materials with positive Poisson's ratio (25).

7- Numerical investigation of patterns behavior

To capture the effect of geometry and material properties on global behavior of a folded shell system, a stiffness analysis can be carried out and the structure can be simulated using a Finite Element Analysis (FEA). Depending on the application, either a constrained bar-framework origami modeling approach (*1, 28*) or a modeling scheme using nonlinear shell elements can be used at this stage. To model folded shell structures, we used the pin-jointed bar framework approach proposed by Schenk and Guest (*1, 28*). In this modeling scheme, fold lines and vertices are modeled with bars and frictionless joints, respectively. To stabilize each facet and to model the bending of the facets for stiffness analysis, the facets are triangulated, and additional members are added to each facet. Placing of additional members is based on observations from physical models, stabilization of the facets, and energetic consideration in facet bending (*1*). This model accounts for bending of the facets and the effect of out-of-plane kinematics of the sheets, and therefore is not restricted to rigid origami.

By varying the ratio of the bending stiffness of the facets and fold lines (K_{facet}/K_{fold}), we performed stiffness analysis for 3x3 patterns of BCH_2 and BCH_3, and 2x3 patterns of the unit cells shown in Fig. S1D with $\alpha=60$ degrees, $a=1$ and $b=2$. The stiffness analysis of the patterns reveals that twisting and bending modes are predominant behavior of the patterns over a large range of K_{facet}/K_{fold} and geometries (Fig. S6-Fig. S8, A and B). The modal shapes corresponding to the lowest eigen-value of the sheets show that for large values of K_{facet}/K_{fold}, the first softest deformation mode represents a rigid origami behavior (Fig. S6-Fig. S8, C).

7-1- Numerical calculation of the number of DOFs of the patterns

In the bar-framework analysis, *compatibility* equation is to relate the nodal displacements $\boldsymbol{d}$ to the bar extensions $\boldsymbol{e}$ via compatibility matrix $\boldsymbol{C}$ as follows

$$\boldsymbol{C}\boldsymbol{d} = \boldsymbol{e} \tag{22}$$

From the above equation, the nullspace of the compatibility matrix provides the solution in which the bars do not extend. To model rigid origami behavior, we need to add an angular constraint to the compatibility matrix whose nullspace can provide the nodal displacements $\boldsymbol{d}$ for which the facets do not bend either. The angular constraint can be written in terms of the dihedral fold angles between triangulated facets connected by added fold lines (*1, 28*). Hence,

$$\boldsymbol{J}_{facet}\,\boldsymbol{d} = d\rho \tag{23}$$

where ρ is the dihedral fold angle between two adjoining triangulated facets and $\boldsymbol{J}_{facet}$ is the Jacobian of the angular constraint considered for the triangulated facets intersecting by added fold lines. Therefore, the augmented compatibility matrix is as follows

$$\bar{\boldsymbol{C}} = \begin{bmatrix} \boldsymbol{C} \\ \boldsymbol{J}_{facet} \end{bmatrix} \tag{24}$$

Accordingly, the number of internal infinitesimal mechanisms (*i.e.*, the number of independent DOFs) can be obtained from the expression

$$m = 3j - rank(\bar{\boldsymbol{C}}) - 6 \tag{25}$$

in which j is the number of joints (*i.e.*, the number of vertices). In the relation above, the 6 DOFs related to the rigid-body motions of 3D structures are excluded.

We use the above relation to obtain the number of DOFs for the patterns considering rigid origami behavior. The results are justified based on the geometry of the patterns as well as existence of the implicit formation of the structure of the Miura-ori cells with one-DOF mechanism as described in Section (3).

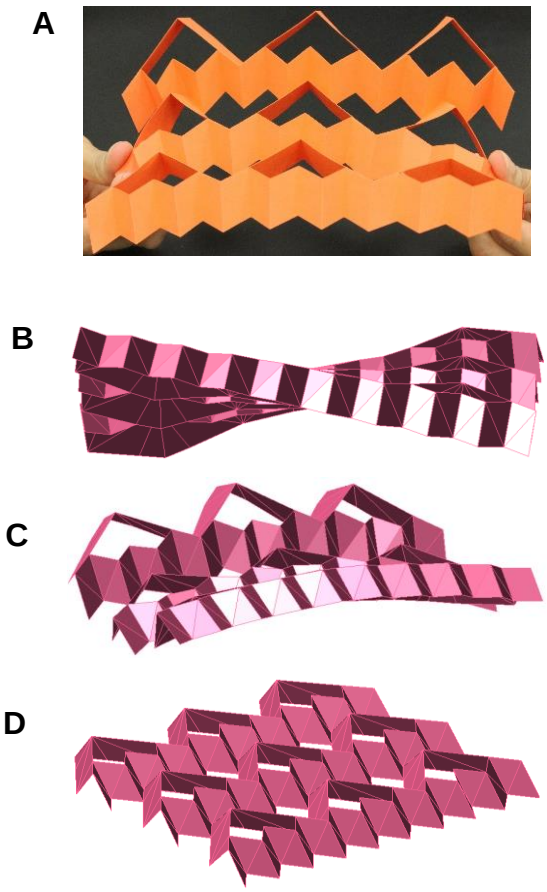

Fig. S6. Behavior of a BCH_3 sheet upon bending and results of the eigenvalue analysis of a 3 × 3 pattern of BCH_3. (**A**) Sheet of BCH_3 deforms into a saddle-shaped under bending which is typical behavior for materials having a positive Poisson's ratio. (**B**) Twisting, (**C**) saddle-shaped and (**D**) rigid origami behavior (planar mechanism) of a 3 by 3 pattern of BCH_3 (with $a=1$; $b=2$; $\alpha = 60^{\circ}$).

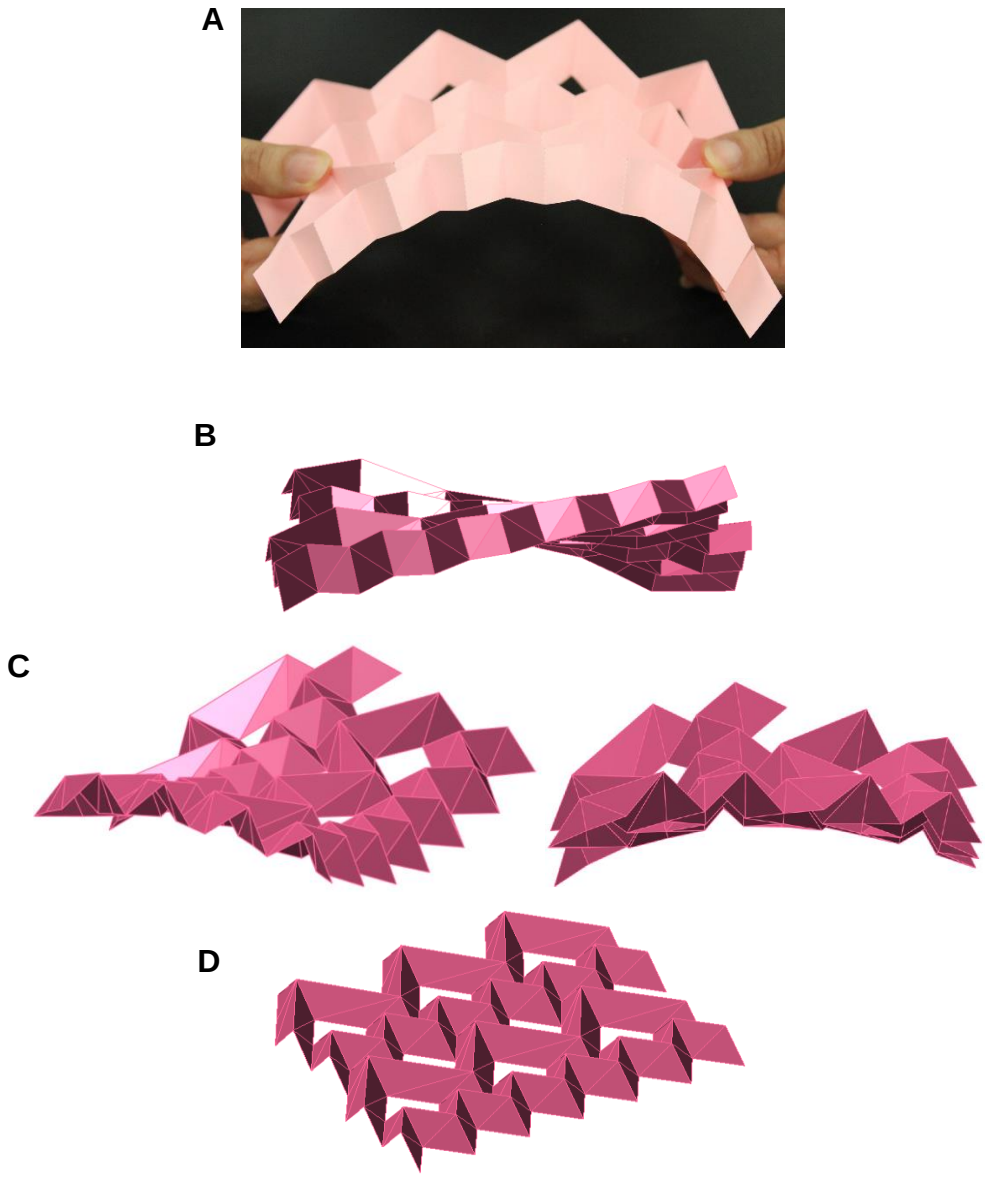

Fig. S7. Behavior of a sheet of the pattern shown in Fig. 3C upon bending and results of eigenvalue analysis of a 2 × 3 sheet of the pattern. (**A**) The sheet deforms into a saddle-shaped under bending (*i.e.*, typical behavior seen in materials having a positive Poisson's ratio). (**B**) Twisting, (**C**) saddle-shaped from two different views and (**D**) rigid origami behavior (planar mechanism) of a 2 by 3 pattern shown in Fig. 3C (with *a=1*; *b=2*; α = 60°).

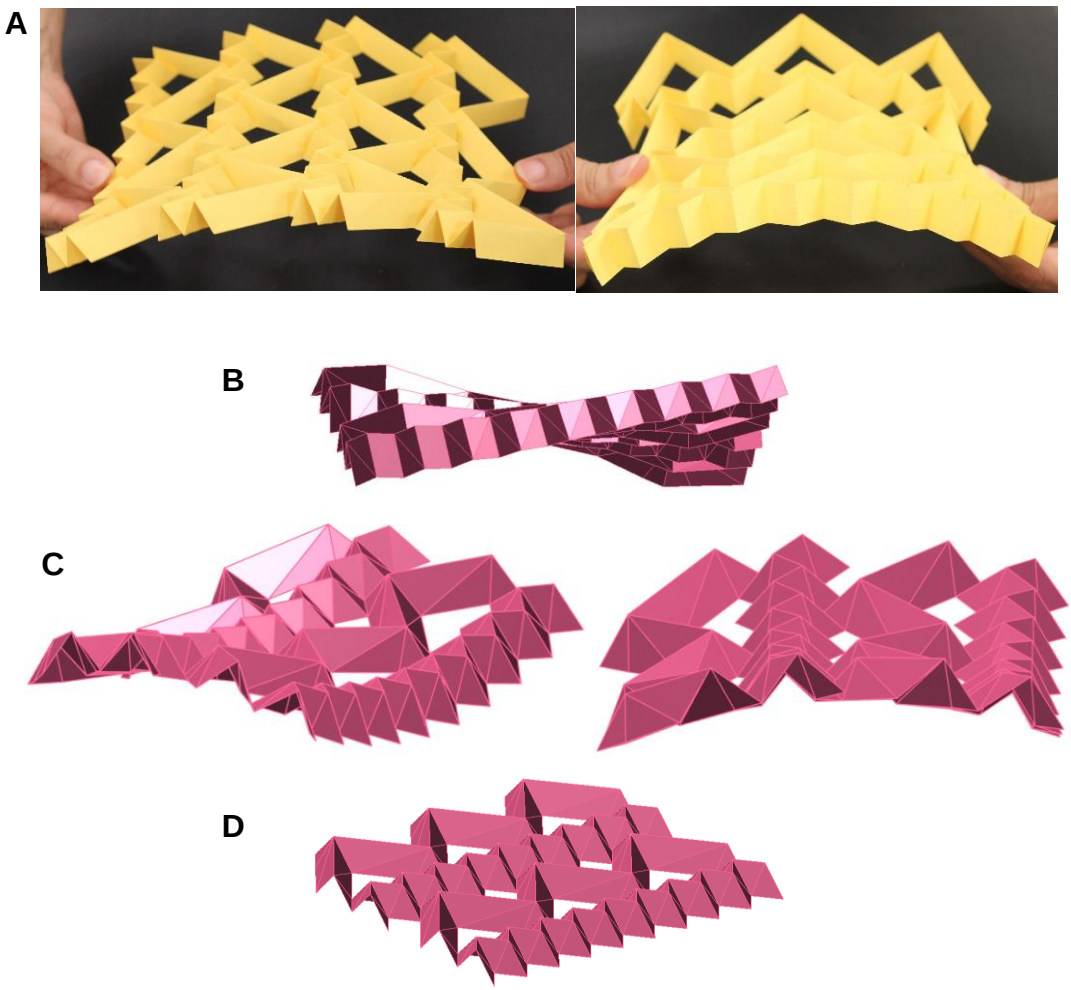

Fig. S8. Behavior of a sheet of the pattern shown in Fig. 3D upon bending and results of eigenvalue analysis of a 2 × 3 sheet of the pattern. (**A**) The sheet deforms into a saddle-shaped under bending, *i.e.* a typical behavior seen in materials having a positive Poisson's ratio. (**B**) Twisting, (**C**) saddle-shaped from two different views and (**D**) rigid origami behavior (planar mechanism) of a 2 by 3 pattern shown in Fig. 3D (with $a=1$; $b=2$; α = 60°).

Movie S1

In-plane behavior of the patterns. The patterns are developable, flat-foldable and rigid-foldable. For most geometric ranges, they exhibit negative Poisson's ratio under extension.

Movie S2

A cellular folded metamaterial made from stacking seven layers of 3×3 sheet of BCH_2 pattern with two different geometries.

Movie S3

Out-of-plane behavior of the patterns. Under bending, the patterns deform into saddle-shaped.